Instability of the isothermal, hydrostatic equatorial atmosphere at rest under the full Coriolis acceleration

Ray Chew[a], Mark Schlutow[b]*, Rupert Klein[a]

[a] FB Mathematik & Informatik
Freie Universität Berlin
Arnimallee 6, 14195 Berlin, Germany

[b] Department Biogeochemical Signals
Max Planck Institute for Biogeochemistry
Hans-Knöll-Str. 10, 07745 Jena, Germany

*Corresponding author: mschlutow@bgc-jena.mpg.de

The traditional approximation neglects the cosine components of the Coriolis acceleration, and this approximation has been widely used in the study of geophysical phenomena. However, the justification of the traditional approximation is questionable under a few circumstances. In particular, dynamics with substantial vertical velocities or geophysical phenomena in the tropics have non-negligible cosine Coriolis terms. Such cases warrant investigations with the non-traditional setting, i.e., the full Coriolis acceleration. In this manuscript, we study the effect of the non-traditional setting on an isothermal, hydrostatic and compressible atmosphere assuming a meridionally homogeneous flow. Employing linear stability analysis, we show that, given appropriate boundary conditions, i.e. free-slip boundary at the surface and non-reflecting boundary at the top, the equatorial atmosphere at rest becomes unstable. Numerical experiments were conducted, and Rayleigh damping is used as a numerical approximation for the non-reflecting top boundary. Our two main results are as follows. 1) Experiments involving the full Coriolis terms exhibit exponentially growing instability while experiments subject to the same initial condition and the traditional approximation remain stable. 2) The experimental instability growth rate is close to the theoretical value. Despite the limitations of our investigations wherein only studies on the f-plane are conducted, and effects from the β-plane approximation are ignored, the presence of this instability may have physical and experimental implications for the non-traditional setting. A discussion of the limitations and implications of our study concludes our investigations. Specifically, the influence on numerical deep-atmosphere models and the validity of assuming meridionally homogeneous flow are discussed.

1. Introduction

The Coriolis force arises from the Earth's rotation. Named after Coriolis [1835], the effect of the Coriolis force is the deflection of a particle moving along the surface of the globe. Such an effect is perpendicular to the axis of the globe's rotation and the direction of the particle's velocity. Atmospheric and oceanic phenomena are subjected to the effects of the Coriolis force. Yet, as the atmosphere and ocean are shallow relative to the Earth's radius, the dynamics we are interested in are largely horizontal.

Based on the argument of the difference in the horizontal and vertical scales of the dynamics, Laplace [1835] concluded that in studying the Coriolis effects, we may neglect the vertical acceleration arising from the Coriolis force, keeping only the horizontal. Specifically, the full Coriolis acceleration results in a tilted outward-pointing vector along the surface of the globe. This vector may be decomposed into sine and cosine components. The former are perpendicular to the surface of the globe and induce only horizontal

motion, while the latter are parallel and associated with vertical motion. Appendix A provides an elaboration on the full Coriolis acceleration. Following the arguments by Laplace, one may drop the cosine terms.

The approximation introduced by Laplace has since been widely used. This led Eckart [1960] to coin the term "traditional approximation" when describing this approximation. The traditional approximation is also introduced in other standard textbooks on atmospheric and oceanic phenomena, see e.g., Pedlosky [2013], Vallis [2017], Achatz [2022]. However, the validity of the traditional approximation may be questioned under certain circumstances. For instance, at the equator where the contributions from the cosine terms are the largest, or for the phenomena involving substantial vertical motion, wherein the vertical Coriolis acceleration should not be ignored.

The limitation of the traditional approximation is gaining increasing attention, and the review by Gerkema et al. [2008] may be a good starting point for a study beyond the traditional approximation. A few other relevant literature are mentioned below. White and Bromley [1995] proposed a set of dynamically-consistent quasi-hydrostatic equations with full Coriolis support. They also demonstrated via scale analysis that, in the tropics, the cosine Coriolis terms may be as large as 10% of the important terms in the equations, and thus they are non-negligible. The condition for linear stability has been derived by Fruman and Shepherd [2008] for a zonally symmetric, compressible and non-traditional setup. They noticed that an instability arises for a particular angular momentum profile near the equator. Fruman [2009] computed the analytical solution for meridionally-confined zonally-propagating waves for the linearised hydrostatic Boussinesq equations including the full Coriolis terms. Studies involving non-traditional effects were also conducted by Colin de Verdière and Schopp [1994], Maas and Harlander [2007], Rodal and Schlutow [2021].

Challenges to the assumptions made in the traditional approximation are not limited to the analysis of physical phenomena. In the example of a numerical model, Borchert et al. [2019] introduced an upper-atmosphere extension to the ICON model [Zängl et al., 2015] that solves the full Coriolis term. Another deep-atmosphere numerical model with full Coriolis support has been published by Smolarkiewicz et al. [2016]. From hereon, we use the term "non-traditional setting" to refer to a setting where the full effect of the Coriolis force is considered.

In this manuscript, we study the stability of an isothermal hydrostatic atmosphere under the non-traditional setting and assuming a meridionally homogeneous flow. Via linear stability analysis of the compressible inviscid Euler equations, we show that, given the non-reflective boundary condition at the top, a small perturbation of the isothermal hydrostatic atmosphere at rest leads to an exponentially-growing instability, and we quantify the theoretical growth rate of this instability. In contrast to the non-reflecting boundary at the top, it can be shown by an argument from functional analysis that the atmosphere is unconditionally stable if a free-slip boundary condition at the top is assumed. Section 2 contains these theoretical developments.

The instability in the case of a non-reflecting upper boundary is investigated through numerical experiments. Section 3 introduces the numerical model by Benacchio and Klein [2019], and Appendix B extends the model to support the non-traditional setting.

The non-reflective top boundary is realised numerically via a Rayleigh damping layer. Experiments made in Section 4 demonstrate that, in the presence of the full Coriolis acceleration, the isothermal, hydrostatic atmosphere at rest becomes unstable with an experimental instability growth rate that is close to the theoretically predicted value. Appendix C extends the investigation from Section 4 to simulation runs over a range of temporal and spatial resolutions.

The existence of this instability due to the full Coriolis effect has two main implications. First, this instability may provide a theoretical understanding of hitherto unexplained physical phenomena. Second, the presence of the instability is relevant to numerical weather and climate prediction models that solve a full representation of the Coriolis force, in particular numerical models of the deep-atmosphere that utilise Rayleigh damping at the top of the atmosphere. Along with a summary of the results of this manuscript, Section 5 provides further elaborations and discussions of these implications. The limitations of assuming meridionally homogeneous flow is also discussed in detail.

2. Theory

2.1. The governing equations

The basis for our investigation are the compressible Euler equations in a rotating coordinate system on the sphere, reproduced below,

$$\frac{D\boldsymbol{v}}{Dt} + c_p\,\theta\nabla\pi + g\,\boldsymbol{e}_z + 2\boldsymbol{\Omega}\times\boldsymbol{v} = 0, \tag{1a}$$

$$\frac{D\theta}{Dt} = 0, \tag{1b}$$

$$\frac{D\pi}{Dt} + \frac{R}{c_v}\,\pi\nabla\cdot\boldsymbol{v} = 0, \tag{1c}$$

where the velocity vector $\boldsymbol{v} = u\,\boldsymbol{e}_x + v\,\boldsymbol{e}_y + w\,\boldsymbol{e}_z$ is composed of the zonal, meridional and vertical wind. The variable $R = c_p - c_v$ denotes the specific gas constant for dry air, where c_p and c_v are the heat capacities at constant pressure and constant volume, respectively. Furthermore, $\boldsymbol{e}_j$, $j \in \{x, y, z\}$ represents the unit vectors, and g is the gravitational acceleration. The Exner pressure π and potential temperature θ are defined by the canonical thermodynamic quantities, temperature T and pressure p. These quantities are related by the equation of states,

$$\pi = (p/p_0)^\kappa, \tag{2a}$$

$$\theta = T/\pi, \tag{2b}$$

with p_0 a reference pressure at $z = 0$ and $\kappa = R/c_p = 2/7$ for two-atomic gases. By means of the ideal gas law, the thermodynamical variables are linked to the density ρ via

$$\rho = \frac{p_0}{R}\frac{\pi^{(1-\kappa)/\kappa}}{\theta}. \tag{3}$$

4

The material derivative is given as

$$\frac{D}{Dt} = \frac{\partial}{\partial t} + \boldsymbol{v} \cdot \nabla \tag{4}$$

where $\nabla = \boldsymbol{e}_x\, \partial/\partial x + \boldsymbol{e}_y\, \partial/\partial y + \boldsymbol{e}_z\, \partial/\partial z$ denotes the nabla operator. Finally, the vector $\boldsymbol{\Omega}$ represents Earth's angular velocity in the direction of the Earth's rotational axis. The governing equations introduced in (1) are based on mass, momentum and energy conservation.

2.2. The non-traditional setting

The effect of the non-traditional setting is most obvious at the equator. Therefore, we assume the f-F-plane at the equator [Thuburn et al., 2002], i.e., $f = 0$ and $F = 2\Omega$ with $\Omega = |\boldsymbol{\Omega}|$. More details on the f-F-plane notation may be found in Appendix A. Also note that we neglect any effects due to the β-plane which is a valid assumption as long as the meridional scale of the flow is small. A justification by means of scale analysis is given in Section 5. From hereon, we consider only the flow in the x-z-plane, i.e. we restrict the analysis to meridionally homogeneous fields. The horizontal domain of interest is $x \in [0, x_{\mathrm{MAX}}]$ with $z \in [0, z_{\mathrm{TOA}}]$ for the vertical extent. Here, 0 represents the height of the Earth's surface without orography, and *TOA* stands for a *fictitious* 'top of the atmosphere', and a clearer elaboration on the boundary conditions will be provided in Subsection 22.4. This problem setup is illustrated in Figure 1.
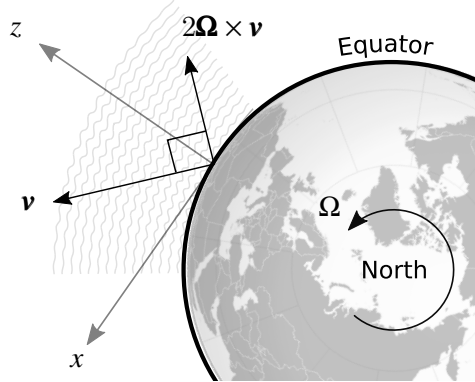

Figure 1: Sketch of the Coriolis acceleration at the equator.

5

Writing out the compact form of (1) explicitly yields the following,

$$\frac{\partial u}{\partial t} + u\frac{\partial u}{\partial x} + w\frac{\partial u}{\partial z} + c_p\theta\frac{\partial \pi}{\partial x} + Fw = 0, \tag{5a}$$

$$\frac{\partial w}{\partial t} + u\frac{\partial w}{\partial x} + w\frac{\partial w}{\partial z} + c_p\theta\frac{\partial \pi}{\partial z} - Fu + g = 0, \tag{5b}$$

$$\frac{\partial \theta}{\partial t} + u\frac{\partial \theta}{\partial x} + w\frac{\partial \theta}{\partial z} = 0, \tag{5c}$$

$$\frac{\partial \pi}{\partial t} + u\frac{\partial \pi}{\partial x} + w\frac{\partial \pi}{\partial z} + \frac{R}{c_v}\pi\left(\frac{\partial u}{\partial x} + \frac{\partial w}{\partial z}\right) = 0. \tag{5d}$$

2.3. The hydrostatic background atmosphere

A stationary solution to the governing equations (5) is the hydrostatic atmosphere at rest, i.e.,

$$u(x, z, t) = 0, \tag{6a}$$

$$w(x, z, t) = 0, \tag{6b}$$

$$\theta(x, z, t) = \bar{\theta}(z), \tag{6c}$$

$$\pi(x, z, t) = \bar{\pi}(z). \tag{6d}$$

Substituting (6) into (1), all governing equations but the vertical velocity equation (5b) vanish. The remaining equation reduces to the hydrostatic equation,

$$c_p\bar{\theta}\frac{d\bar{\pi}}{dz} = -g. \tag{7}$$

Given a temperature profile $\bar{T} = \bar{T}(z)$, we can integrate (7) using the definitions in (2) to obtain the hydrostatic background variables, and they may be written as follows,

$$\bar{\pi}(z) = \exp\left[-\int_0^z \frac{g}{c_p}\frac{1}{\bar{T}(\zeta)}d\zeta\right], \tag{8}$$

$$\bar{\theta}(z) = T_0\exp\left[\int_0^z \frac{1}{\bar{T}(\zeta)}\left(\frac{g}{c_p} + \frac{d\bar{T}}{d\zeta}\right)d\zeta\right], \tag{9}$$

$$\bar{\rho}(z) = \frac{p_0}{RT_0}\exp\left[-\int_0^z \frac{1}{\bar{T}(\zeta)}\left(\frac{g}{R} + \frac{d\bar{T}}{d\zeta}\right)d\zeta\right]. \tag{10}$$

Subsequently, we consider perturbations from the basic, hydrostatic state by the following ansatz,

$$u(x, z, t) = u'(x, z, t), \tag{11a}$$

$$w(x, z, t) = w'(x, z, t), \tag{11b}$$

$$\theta(x, z, t) = \bar{\theta}(z) + \theta'(x, z, t), \tag{11c}$$

$$\pi(x, z, t) = \bar{\pi}(z) + \pi'(x, z, t). \tag{11d}$$

Assuming that the perturbations are infinitesimally small, we may linearise the governing equations around the basic hydrostatic state. Before stating the linearised system, we introduce a transformation that simplifies the upcoming derivations [cf. Achatz et al., 2010, Eq. 2.16],

$$\hat{u} = \bar{\rho}^{1/2}\, u', \tag{12a}$$

$$\hat{w} = \bar{\rho}^{1/2}\, w', \tag{12b}$$

$$\hat{\theta} = \frac{g}{N}\, \bar{\rho}^{1/2}\, \bar{\theta}^{-1}\, \theta', \tag{12c}$$

$$\hat{\pi} = \frac{c_p}{C}\, \bar{\rho}^{1/2}\bar{\theta}\, \pi'. \tag{12d}$$

Here, the Brunt-Väisälä frequency and the speed of sound are given by

$$N(z) = \sqrt{\frac{g}{\bar{\theta}(z)}\frac{\mathrm{d}\bar{\theta}}{\mathrm{d}z}} = \sqrt{\frac{g}{\bar{T}(z)}\left(\frac{g}{c_p} + \frac{\mathrm{d}\bar{T}}{\mathrm{d}z}\right)}, \tag{13}$$

$$C(z) = \sqrt{\gamma R \bar{T}(z)}, \quad \gamma = \frac{c_p}{c_v}, \tag{14}$$

respectively. Inserting (12) into (11) and the result into (5), we may write the linearised system in terms of the transformed perturbation variables as

$$\frac{\partial \hat{u}}{\partial t} + \frac{\partial}{\partial x}\left(C\hat{\pi}\right) + F\hat{w} = 0, \tag{15a}$$

$$\frac{\partial \hat{w}}{\partial t} + \left(\frac{\partial}{\partial z} + \Gamma\right)\left(C\hat{\pi}\right) - N\hat{\theta} - F\hat{u} = 0, \tag{15b}$$

$$\frac{\partial \hat{\theta}}{\partial t} + N\hat{w} = 0, \tag{15c}$$

$$\frac{\partial \hat{\pi}}{\partial t} + C\left[\frac{\partial \hat{u}}{\partial x} + \left(\frac{\partial}{\partial z} - \Gamma\right)\hat{w}\right] = 0, \tag{15d}$$

where we introduced the quantity Γ as

$$\Gamma(z) = -\frac{1}{2\bar{\rho}(z)}\frac{\mathrm{d}\bar{\rho}}{\mathrm{d}z} - \frac{1}{\bar{\theta}(z)}\frac{\mathrm{d}\bar{\theta}}{\mathrm{d}z}$$

$$= \frac{1}{2\bar{T}(z)}\left[\left(\frac{c_v}{R} - 1\right)\frac{g}{c_p} - \frac{\mathrm{d}\bar{T}}{\mathrm{d}z}\right] \tag{16}$$

in accordance with Durran [1989]. Notice that by the choice of the variable transformation,

$$E = \frac{1}{2}\left(\hat{u}^2 + \hat{w}^2 + \hat{\theta}^2 + \hat{\pi}^2\right) \tag{17}$$

is the total energy density of the perturbation which evolves in time as

$$\frac{\partial E}{\partial t} + \frac{\partial}{\partial x}\left(C\hat{u}\hat{\pi}\right) + \frac{\partial}{\partial z}\left(C\hat{w}\hat{\pi}\right) = 0. \tag{18}$$

Hence, Gauss' theorem ensures that the total energy is locally conserved. The quantity $\hat{u}^2 + \hat{w}^2$ represents the kinetic energy density of the perturbation, and the quantities $\hat{\theta}^2$ and $\hat{\pi}^2$ are the potential and internal energy density, respectively.

2.4. Linear stability analysis

Let us denote the vector of prognostic variables by $\hat{\boldsymbol{\psi}} = (\hat{u}, \hat{w}, \hat{\theta}, \hat{\pi})^{\mathrm{T}}$, and notice that the solution of the linearised equations (15) is of the form

$$\hat{\boldsymbol{\psi}}(x, z, t) = \boldsymbol{\psi}(x, z) \exp(-i\lambda t), \quad \lambda \in \mathbb{C}. \tag{19}$$

The ansatz yields an eigenvalue problem with eigenvalues $i\lambda$, i.e.,

$$(\mathbf{T} - i\lambda)\boldsymbol{\psi} = 0, \tag{20}$$

with the differential operator

$$\mathbf{T} = \begin{pmatrix} 0 & F & 0 & \partial/\partial x(C \cdot) \\ -F & 0 & -N & \partial/\partial z(C \cdot) + \Gamma C \\ 0 & N & 0 & 0 \\ C\partial/\partial x & C\partial/\partial z - C\Gamma & 0 & 0 \end{pmatrix}. \tag{21}$$

Note that $\boldsymbol{\psi}$ is complex valued, and the solution of (20) is a linear combination of the eigenfunctions. This ensures that the solutions are eventually real fields.

Now, let us define an inner product as

$$\langle \boldsymbol{\psi} | \boldsymbol{\phi} \rangle = \int_0^{z_{\mathrm{TOA}}} \int_0^{x_{\mathrm{MAX}}} \boldsymbol{\psi}^{\mathrm{H}} \boldsymbol{\phi} \, \mathrm{d}x \mathrm{d}z \tag{22}$$

in terms of some well-behaved vectors of prognostic variables $\boldsymbol{\psi} = (\psi_u, \psi_w, \psi_\theta, \psi_\pi)^{\mathrm{T}}$ and $\boldsymbol{\phi} = (\phi_u, \phi_w, \phi_\theta, \phi_\pi)^{\mathrm{T}}$ that satisfy the yet to be defined boundary conditions. Furthermore, H denotes the Hermitian transpose, i.e the complex conjugated and transposed. This inner product induces a norm that is given as

$$\|\boldsymbol{\psi}\|^2 = \langle \boldsymbol{\psi} | \boldsymbol{\psi} \rangle = \int_0^{z_{\mathrm{TOA}}} \int_0^{x_{\mathrm{MAX}}} \boldsymbol{\psi}^{\mathrm{H}} \boldsymbol{\psi} \, \mathrm{d}x \mathrm{d}z = \int_0^{z_{\mathrm{TOA}}} \int_0^{x_{\mathrm{MAX}}} 2\,E \, \mathrm{d}x \mathrm{d}z, \tag{23}$$

which corresponds to twice the global energy. Hence, this choice of the inner product also has a physical motivation.

At this point, an open question is the choice of realistic boundary conditions. To answer this question, we consider the properties of the operator $\mathbf{T}$. If we assume for simplicity periodic boundary conditions in the x-directions, such that $\boldsymbol{\psi}(0, z) = \boldsymbol{\psi}(x_{\mathrm{MAX}}, z)$ (or vanishing fields at $x \to \pm\infty$), we then observe that

$$\langle \mathbf{T}\boldsymbol{\psi} | \boldsymbol{\phi} \rangle = -\langle \boldsymbol{\psi} | \mathbf{T}\boldsymbol{\phi} \rangle + \int_0^{x_{\mathrm{MAX}}} \left[C\psi_\pi^* \phi_w + C\psi_w^* \phi_\pi \right]_0^{z_{\mathrm{TOA}}} \mathrm{d}x \tag{24}$$

for all $\boldsymbol{\psi}$ and $\boldsymbol{\phi}$. Here, $*$ denotes the complex conjugate. This observation implies that the operator $\mathbf{T}$ is skew-Hermitian if the following condition holds,

$$\left[C\psi_\pi^* \phi_w + C\psi_w^* \phi_\pi \right]_0^{z_{\text{TOA}}} = 0. \tag{25}$$

Skew-Hermitian operators exhibit purely imaginary eigenvalues $i\lambda$ (or rather an imaginary spectrum to be precise), so $\lambda \in \mathbb{R}$. Therefore, the perturbation is bounded in time and ultimately stable if the condition in (25) holds.

Whether or not condition (25) holds now depends on the choice of the vertical boundaries. For the bottom surface with no orography, we assume a free-slip (no-normal-flow) boundary, i.e. $w(x, 0, t) = 0$. This boundary condition implies that

$$\psi_w, \phi_w = 0 \quad \text{at } z = 0. \tag{26}$$

If we were to also restrict the fields to vanish at the upper boundary, then the condition (25) holds, and all perturbations would be stable. A similar result generalised to the equatorial β-plane was also obtained by Fruman and Shepherd [2008] who considered zonally symmetric flows. However, since the top of the atmosphere cannot be clearly defined, and the boundary conditions remain a means to obtain a tractable model, we will assume a free surface at $z = z_{\text{TOA}}$. This boundary condition is also known as a *non-reflecting boundary.*

With a non-reflecting boundary, condition (25) no longer holds, and this leads to interesting behaviour of the perturbations in (15). In reality, dissipation increases with height such that any perturbation would be damped to zero above a certain altitude. However, the incorporation of height-dependent dissipation into our model would render it intractable for analytic progress, and we argue that the free surface is a worthwhile alternative for this study. Furthermore, while non-reflecting upper boundaries may be physically unrealistic, they are common practice in numerical weather and climate models including deep-atmosphere non-traditional models [Smolarkiewicz et al., 2016, Borchert et al., 2019]. Subsequent investigations in this paper will assume a free surface for the top boundary. The non-reflective upper boundary is modelled numerically with a Rayleigh damping layer, and more details will be provided in Section 4.

2.5. The isothermal background atmosphere

Let us simplify our model even further by assuming an isothermal background state, $\partial \bar{T} / \partial z = 0$. As a consequence, all coefficients in $\mathbf{T}$ become constant and, taking the horizontal boundary conditions into account, the perturbation must be of the form

$$\boldsymbol{\psi}(x, z) = \tilde{\boldsymbol{\psi}} \exp(ikx + \mu z), \quad k \in \mathbb{R}, \mu \in \mathbb{C}. \tag{27}$$

The operator $\mathbf{T}$ may be written as a matrix, that is,

$$\tilde{\mathbf{T}} = \begin{pmatrix} 0 & F & 0 & iCk \\ -F & 0 & -N & C(\mu + \Gamma) \\ 0 & N & 0 & 0 \\ iCk & C(\mu - \Gamma) & 0 & 0 \end{pmatrix}. \tag{28}$$

Dividing (28) by N, the system may be non-dimensionalised by defining new dimensionless variables that are given as follows,

$$K = \frac{C}{N} k, \quad M = \frac{C}{N} \mu, \quad \Lambda = \frac{1}{N} \lambda, \quad \varepsilon = \frac{F}{N}. \tag{29}$$

The eigenvalue problem of (20) written in terms of the dimensionless variables, and incorporating the horizontal periodic boundary conditions, leads to

$$(\mathbf{S} - i\Lambda)\, \tilde{\boldsymbol{\psi}} = 0, \quad \mathbf{S}(K, M; \varepsilon) = \begin{pmatrix} 0 & \varepsilon & 0 & iK \\ -\varepsilon & 0 & 1 & M+G \\ 0 & -1 & 0 & 0 \\ iK & M-G & 0 & 0 \end{pmatrix}, \tag{30}$$

where we have

$$G = \frac{C\Gamma}{N} = \sqrt{\frac{9}{40}}. \tag{31}$$

The characteristic polynomial of $\mathbf{S}$ is obtained as,

$$\mathcal{P}_{\mathbf{S}(K,M;\varepsilon)}(i\Lambda) = \Lambda^4 - \left(1 + \varepsilon^2 + G^2 + K^2 - M^2\right)\Lambda^2 + 2\varepsilon\, GK\Lambda + K^2. \tag{32}$$

This polynomial is a depressed quartic function in Λ. On the one hand, its roots can be expressed by radicals. However, the expressions would be tedious providing no further enlightenment. On the other hand, we note that typically $\varepsilon = O\left(10^{-2}\right)$ is a very small number. Therefore, it is sensible to employ perturbation theory instead. If we assume that $M, K = O(1)$ as $\varepsilon \to 0$, then to leading-order, we have as roots to the characteristic polynomials

$$\Lambda^{(0)\,2} = \frac{1}{2}L^2\left(1 \pm \sqrt{1 - 4\frac{K^2}{L^4}}\right), \tag{33}$$

$$L^2 = K^2 - M^2 + 1 + G^2 = K^2 - M^2 + \frac{49}{40}, \tag{34}$$

which is essentially the dispersion relation for acoustic-gravity waves.

2.6. The leading-order eigenvector

Computing the leading-order eigenvector of $\mathbf{S}(K, M; 0)$ gives us

$$\tilde{\boldsymbol{\psi}}^{(0)} = \left(1,\ \frac{i}{K}\frac{K^2 - \Lambda^{(0)\,2}}{M+G},\ -\frac{1}{\Lambda^{(0)}K}\frac{K^2 - \Lambda^{(0)\,2}}{M+G},\ \frac{\Lambda^{(0)}}{K}\right)^{\mathrm{T}}, \tag{35}$$

and (35) fulfills non-trivially the lower boundary condition $\psi_w = 0$ at $z = 0$ if

$$\Lambda^{(0)\,2} = K^2. \tag{36}$$

Substituting (36) into (32), we can solve the leading-order characteristic polynomial to obtain

$$M = G, \tag{37}$$

and hence the leading-order eigenvector becomes

$$\tilde{\boldsymbol{\psi}}^{(0)} = \left(1, \ 0, \ 0, \ \pm 1\right)^{\mathrm{T}}. \tag{38}$$

This solution is equivalent to a Lamb wave [Vallis, 2017]. Since the characteristic polynomial is a quartic, we expect to find four roots. For the free-slip lower boundary condition we imposed, we obtained only two roots in (36). The leading-order polynomial has two more roots for $M = G$ that do not satisfy the boundary condition, and these are

$$\Lambda^{(0)\,2} = 1. \tag{39}$$

These roots would be equivalent to Brunt waves [Walterscheid, 2003], if our boundaries were to allow for them.

2.7. The instability growth rate

Figure 2 depicts all four leading-order roots (gray lines) for varying horizontal wavenumber K. Notice that, to leading order, we obtain only real-valued roots, and these translate
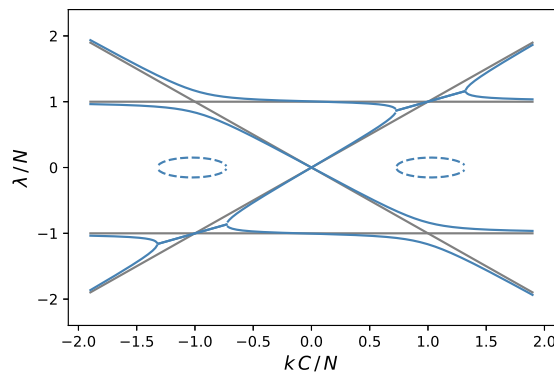

Figure 2: Leading-order roots of the characteristic polynomial $\mathcal{P}_{\mathbf{S}(K,G;\,0)}\left(i\Lambda^{(0)}\right)$ (gray lines, see (32)). Real part of the numerically computed roots of $\mathcal{P}_{\mathbf{S}(K,G;\,0.1)}(i\Lambda)$ (solid blue line) and its imaginary part (dashed blue line) for $\varepsilon = 0.1$. We chose an unrealistically large ε in order to exemplify its effect.

to purely imaginary and hence stable eigenvalues (spectrum). However, the numerical solution for $\varepsilon \neq 0$ reveals imaginary parts for Λ (the dashed blue lines) and, consequentially, the perturbations might be unstable in these regions. With reference to Figure 2, we observe that the potentially unstable eigenvalues appear around $K = kC/N = \pm 1$.

This point is distinct as the leading-order operator degenerates: its eigenvalues have algebraic multiplicity of two instead of one at this point.

We now determine the maximum imaginary part of Λ, and this gives us the instability growth rate of the perturbation. This entails solving for an asymptotic solution at the point of degeneracy, $K = \pm 1$. However, perturbation theory for non-Hermitian operators that have leading-order eigenvalues with algebraic multiplicity greater than one is in fact cumbersome [Kato, 1982]. Its rigorous mathematical treatment is beyond the scope of this paper as standard techniques from, say, quantum mechanics are inapplicable. That being the case, we will nevertheless provide an asymptotic analysis of the next-order correction to the eigenvalue, while refraining from the more involved computations for the eigenvectors. For this purpose, we expand Λ in terms of powers of ε,

$$\Lambda = \Lambda^{(0)} + \varepsilon^{1/2}\Lambda^{(1/2)} + o(\varepsilon^{1/2}). \tag{40}$$

The choice for the exponent of $1/2$ for the next-to-leading-order term is due to the multiplicity of the eigenvalue. The interested reader finds a complete reasoning on this matter in Lidskii [1966]. Also, Kato [1982] contains a proof on the existence and form of the expansion. Substituting the ansatz together with the leading-order result in the characteristic polynomial (32) and collecting terms of the same power in ε, we find that terms, which are of $O(\varepsilon^{1/2})$, cancel each other. At $O(\varepsilon)$, we obtain

$$\Lambda^{(1/2)} = \pm i\sqrt{\frac{G}{2}}. \tag{41}$$

Rewriting (41) together with the leading-order result in a dimensional form yields

$$\lambda \approx \pm N \pm i\sqrt{\frac{F}{2}C\Gamma} \tag{42}$$

and hence the instability growth rate is given as $\sqrt{\Omega C\Gamma}$.

Summarising this section, we found a linearly unstable meridionally homogeneous mode of the hydrostatic atmosphere at rest at the equator by means of asymptotic perturbation theory. The mode is to leading order identical to Lamb waves which are a known horizontally propagating external mode of the atmosphere. Its phase velocity is the speed of sound. Note that the boundary conditions of the unstable mode are fulfilled to leading order. We derived a higher-order correction to the eigenvalues of the linearised system and argued that a derivation of the corresponding correction to the eigenvector is beyond the scope of this paper. As a consequence, it remains unclear if such a next-order eigenvector would equally fulfil the boundary conditions.

The validity of our asymptotic theory is therefore tested against the numerical solution of the nonlinear governing equations in the next section.

3. Numerical Model

The numerical corroboration of the Lamb-wave-like instability, that we derived in the previous section, necessitates a model that is capable of solving the compressible non-

hydrostatic Euler equations. The numerical model by Benacchio and Klein [2019] is well-tested and meets our requirements. It is especially suitable to study flow instabilities numerically due to its conservation characteristics and numerical stability properties. The numerical model is second-order accurate and semi-implicit.

In the following, we give a brief summary of the model. The governing adiabatic compressible equations with constant heat capacities under the influence of gravity and in a rotating coordinate system corresponding to a non-traditional tangent-plane approximation are given by

$$\frac{\partial \rho}{\partial t} + \nabla_\parallel \cdot (\rho \boldsymbol{u}) = 0, \tag{43a}$$

$$\frac{\partial (\rho \boldsymbol{u})}{\partial t} + \nabla_\parallel \cdot (\rho \boldsymbol{u} \circ \boldsymbol{u}) + \frac{\partial (\rho w \boldsymbol{u})}{\partial z} = -\left[c_p P \nabla_\parallel \pi + (2 \boldsymbol{\Omega} \times \rho \boldsymbol{v})_\parallel \right], \tag{43b}$$

$$\frac{\partial (\rho w)}{\partial t} + \nabla_\parallel \cdot (\rho \boldsymbol{u} w) + \frac{\partial (\rho w^2)}{\partial z} = -\left[c_p P \frac{\partial \pi}{\partial z} + \rho g + (2 \boldsymbol{\Omega} \times \rho \boldsymbol{v})_\perp \right], \tag{43c}$$

$$\frac{\partial P}{\partial t} + \nabla_\parallel \cdot (P \boldsymbol{u}) + \frac{\partial (P w)}{\partial z} = 0. \tag{43d}$$

Here, $\boldsymbol{u} = u \boldsymbol{e}_x + v \boldsymbol{e}_y$ is the velocity vector of the zonal and meridional wind, and

$$P = \frac{p_0}{R} \left(\frac{p}{p_0} \right)^{\frac{c_v}{c_p}} \equiv \rho \theta \tag{44}$$

is the mass-weighted potential temperature. The operator $\nabla_\parallel = \boldsymbol{e}_x \, \partial/\partial x + \boldsymbol{e}_y \, \partial/\partial y$ subsumes the horizontal partial derivatives, and $\boldsymbol{q}_\parallel$, $\boldsymbol{q}_\perp$ are the horizontal and vertical components of the vector $\boldsymbol{q}$.

Multiplying the governing equations (1) with ρ leads to (43), wherein the evolution equation of the Exner pressure π in (1c) is now subsumed under the evolution equation for P, i.e. (43d). This particular formulation of the governing equations in (43) facilitates the subsequent discussion on the numerical model.

3.1. Compact description of the time integration scheme

In this section, we describe the main structural features of the discretisation following Benacchio et al. [2014], Benacchio and Klein [2019]. A summary of the numerical model is also provided in Chew et al. [2022a].

3.1.1. Reformulation of the governing equations

The primary unknowns advanced in time are the same as in (43), i.e. $(\rho, \rho \boldsymbol{u}, \rho w, P)$. Moreover, the inverse of the potential temperature is introduced as

$$\chi = 1/\theta, \tag{45}$$

such that (43a) becomes a transport equation for χ,

$$\frac{\partial \rho}{\partial t} + \nabla_\parallel \cdot (\rho \boldsymbol{u}) + \frac{\partial (\rho w)}{\partial z} = \frac{\partial (P \chi)}{\partial t} + \nabla_\parallel \cdot (P \chi \boldsymbol{u}) + \frac{\partial (P \chi w)}{\partial z} = 0, \tag{46}$$

13

with $(P\boldsymbol{v})$ the advecting flux. The governing equations now read as

$$\frac{\partial \rho}{\partial t} + \nabla_{\parallel} \cdot (P\boldsymbol{u}\chi) + \frac{\partial(Pw\chi)}{\partial z} = 0, \tag{47a}$$

$$\frac{\partial(\rho\boldsymbol{u})}{\partial t} + \nabla_{\parallel} \cdot (P\boldsymbol{u} \circ \chi\boldsymbol{u}) + \frac{\partial(Pw\chi\boldsymbol{u})}{\partial z} = -\left[c_p P \nabla_{\parallel} \pi + (2\boldsymbol{\Omega} \times \rho\boldsymbol{v})_{\parallel}\right], \tag{47b}$$

$$\frac{\partial(\rho w)}{\partial t} + \nabla_{\parallel} \cdot (P\boldsymbol{u}\chi w) + \frac{\partial(Pw\chi w)}{\partial z} = -\left[c_p P \frac{\partial \pi}{\partial z} + \rho g + (2\boldsymbol{\Omega} \times \rho\boldsymbol{v})_{\perp}\right], \tag{47c}$$

$$\frac{\partial P}{\partial t} + \nabla_{\parallel} \cdot (P\boldsymbol{u}) + \frac{\partial(Pw)}{\partial z} = 0. \tag{47d}$$

3.1.2. Auxiliary perturbation variables

To facilitate the formulation of a semi-implicit discretisation with respect to gravity and sound propagation, Benacchio and Klein [2019] make use of the perturbation of the Exner pressure π and the potential temperature variable χ via

$$\pi(t, \boldsymbol{x}, z) = \pi'(t, \boldsymbol{x}, z) + \bar{\pi}(z) \qquad \text{and} \qquad \chi(t, \boldsymbol{x}, z) = \chi'(t, \boldsymbol{x}, z) + \bar{\chi}(z), \tag{48}$$

where the former equation is reproduced from (11d) and with

$$\frac{\mathrm{d}\bar{\pi}}{\mathrm{d}z} = -\frac{g}{c_p}\bar{\chi} \qquad \text{and} \qquad \bar{\pi}(0) = 1 \tag{49}$$

describing the hydrostatically balanced background.

Since, in dimensionless form, $P = \pi^{\gamma-1}$ is a function of the Exner pressure alone, see (44), and as $\bar{\pi}$ is time-independent, one finds from (47d) that

$$\left(\frac{\partial P}{\partial \pi}\right)\frac{\partial \pi'}{\partial t} = -\nabla \cdot [P(\pi)\boldsymbol{v}], \tag{50}$$

whereas the perturbation potential temperature variable χ' follows

$$\frac{\partial(P\chi')}{\partial t} + \nabla_{\parallel} \cdot (P\boldsymbol{u}\chi') + \frac{\partial(Pw\chi')}{\partial z} = -Pw\frac{\partial\bar{\chi}}{\partial z}. \tag{51}$$

Discretisation of (50) and (51) will facilitate the semi-implicit integration of the full variable equations (47). As in Benacchio and Klein [2019], (50) is solved redundantly parallel to (47d).

Following the notation introduced by Smolarkiewicz et al. [2014], we let

$$\boldsymbol{\Psi} = (\chi, \chi\boldsymbol{u}, \chi w, \chi'), \tag{52}$$

and summarise (47) and (51) as

$$\frac{\partial(P\boldsymbol{\Psi})}{\partial t} + \mathscr{A}(\boldsymbol{\Psi}; P\boldsymbol{v}) = Q(\boldsymbol{\Psi}; P), \tag{53a}$$

$$\frac{\partial P}{\partial t} + \nabla \cdot (P\boldsymbol{v}) = 0, \tag{53b}$$

14

while (50), being equivalent to (53b), is not listed separately. In (53), $\mathscr{A}$ represents the update from a suitable advection scheme, and $Q(\boldsymbol{\Psi}; P)$ describes the effect of the right-hand side of (47) on $\boldsymbol{\Psi}$ given P.

3.2. Semi-implicit time discretisation

3.2.1. Implicit midpoint pressure update and advective fluxes

Equation (47d) is discretised with the midpoint rule, i.e.,

$$(P^{n+1} - P^n) = -\Delta t \, \tilde{\nabla} \cdot (P\boldsymbol{v})^{n+1/2}. \tag{54}$$

Note that $\tilde{\nabla}\cdot$ is the discrete approximation of the divergence operator.

The update step (54) requires the advective fluxes at the half-time level, $(P\boldsymbol{v})^{n+1/2}$. This is computed via an explicit advection followed by a linearly implicit discretisation of the remaining and potentially stiff terms. The advection substep is given by

$$(P\boldsymbol{\Psi})^{\#} = \mathscr{A}_{1\text{st}}^{\Delta t/2}(\boldsymbol{\Psi}^n; (P\boldsymbol{v})^n), \tag{55a}$$

$$P^{\#} = P^n - \frac{\Delta t}{2}\tilde{\nabla} \cdot (P\boldsymbol{v})^n, \tag{55b}$$

where $\mathscr{A}_{1\text{st}}^{\Delta t/2}$ corresponds to an at least first-order accurate advection scheme. A more detailed explanation on this half-time update is provided in § 3b1 of Benacchio and Klein [2019].

The $(P\boldsymbol{v})^{n+1/2}$ field is then obtained from an implicit Euler substep for the stiff subset of equations,

$$(P\boldsymbol{\Psi})^{n+1/2} = (P\boldsymbol{\Psi})^{\#} + \frac{\Delta t}{2}Q(\psi^{n+1/2}; P^{n+1/2}), \tag{56a}$$

$$P^{n+1/2} = P^n - \frac{\Delta t}{2}\tilde{\nabla} \cdot (P\boldsymbol{v})^{n+1/2}. \tag{56b}$$

Here, (56b) is an implicit Euler update and thus is part of the implicit midpoint rule for P. The relation between P and π is approximated through a linearisation of the equation of state (44),

$$P^{n+1/2} = P^n + \left(\frac{\tilde{\partial}P}{\tilde{\partial}\pi}\right)^{\#}\left(\pi^{n+1/2} - \pi^n\right), \tag{57}$$

which leads to a linear elliptic equation for $\pi^{n+1/2}$. Here, $\tilde{\partial}$ is the discrete partial derivative.

3.2.2. Implicit trapezoidal rule for the advected quantities

Given $(P\boldsymbol{v})^{n+1/2}$, the semi-implicit time step for $\boldsymbol{\Psi}$ reads

$$(P\boldsymbol{\Psi})^* = (P\boldsymbol{\Psi})^n + \frac{\Delta t}{2}Q(\boldsymbol{\Psi}^n; P^n), \tag{58a}$$

$$(P\boldsymbol{\Psi})^{**} = \mathscr{A}_{\mathrm{2nd}}^{\Delta t}(\boldsymbol{\Psi}; (P\boldsymbol{v})^{n+1/2}), \tag{58b}$$

$$(P\boldsymbol{\Psi})^{n+1} = (P\boldsymbol{\Psi})^{**} + \frac{\Delta t}{2}Q(\boldsymbol{\Psi}^{n+1}; P^{n+1}), \tag{58c}$$

$$P^{n+1} = P^n - \Delta t\tilde{\nabla}\cdot(P\boldsymbol{v})^{n+1/2}. \tag{58d}$$

More details on the full-time update step in (58) is given in §3b2 of Benacchio and Klein [2019], while discretisation details of the second-order advection scheme in (58b) are given §4a and §4b. Details on the discretisation of the semi-implicit integration of the stiff terms in (58c) and (58d), and in particular the extension to support the non-traditional setting, are documented in Appendix B.

4. Numerical Experiment and Results

4.1. The initial condition

The leading-order eigenfunction vector (38) from Section 2 with the non-traditional setting serves as the initial condition for the numerical experiments. Re-dimensionalising (38) in terms of (29) and inserting the result into (27) yields the initial fields at $t = 0$,

$$u' = A\sqrt{\frac{\rho_0}{\bar{\rho}(z)}}\exp(-\Gamma z)\,\cos\left(\frac{N}{C}x\right), \tag{59a}$$

$$w' = 0, \tag{59b}$$

$$\theta' = 0, \tag{59c}$$

$$\pi' = A\frac{C}{c_p}\sqrt{\frac{\rho_0}{\bar{\rho}(z)}}\bar{\theta}^{-1}(z)\exp(-\Gamma z)\,\cos\left(\frac{N}{C}x\right), \tag{59d}$$

where $A = 10^{-3}$ is a prescribed small amplitude. Furthermore, the background density is given as

$$\bar{\rho}(z) = \rho_0\exp(-z/H_\rho), \tag{60}$$

with $H_\rho = RT_0/g$ representing the density scale height. The expression for Γ in (16) simplifies to

$$\Gamma = \frac{1}{H_\rho}\left(\frac{1}{\gamma} - \frac{1}{2}\right) \tag{61}$$

under the assumption of an isothermal atmosphere, and the background potential temperature is

$$\bar{\theta}(z) = \theta_0\exp(z/H_\theta), \tag{62}$$

16

where $H_\theta = H_\rho/\kappa$ denotes the potential temperature scale height. The quantities ρ_0, T_0, and θ_0 are reference density, temperature, and potential temperature at $z = 0$ respectively. The initial density field is obtained via the equation of state (3).

Given an isothermal atmosphere such that $\bar{T}(z) \equiv T_0 = 300\,\text{K}$, $\gamma = 1.4$, $g \approx 9.81\,\text{m}\,\text{s}^{-1}$, $\Omega \equiv \Omega_y = 7.292 \times 10^{-5}\,\text{s}^{-1}$ and $R = 287.4\,\text{J}\,\text{kg}^{-1}\,\text{K}^{-1}$, we obtain a theoretical instability growth rate from (42) with

$$\sqrt{\Omega C \Gamma} \approx 7.85 \times 10^{-4}\,\text{s}^{-1}. \tag{63}$$

This instability growth rate corresponds to a doubling period of the perturbation's amplitude approximately every 15 min. The horizontal extent of the domain is chosen such that it is equivalent to four wavelengths, i.e., $x_{\text{MAX}} = 2\pi j C/N$ with $j = 4$, and this corresponds to $x \in [-244.5\,\text{km}, 244.5\,\text{km}]$. The full vertical extent of the domain corresponds to $z \in [0.0, 80.0\,\text{km}]$.

4.2. Numerical representation of the boundary conditions

To emulate a free surface at the top of the boundary, a wave-absorbing layer is applied to the top 20 km to approximate the non-reflecting boundary condition [Durran, 2010]. Specifically, the Rayleigh damping by Durran and Klemp [1983], as reproduced below, has been used. The following terms are added to the right-hand side of the governing equations in (47),

$$R_u = \tau(z)u, \tag{64a}$$

$$R_w = \tau(z)w, \tag{64b}$$

$$R_\theta = \tau(z)(\theta - \bar{\theta}), \tag{64c}$$

with

$$\tau(z) = \begin{cases} 0 & \text{for } z \leq z_D, \\ -\frac{\alpha}{2}\left[1 - \cos\left(\frac{z-z_D}{z_{\text{TOA}}-z_D}\pi\right)\right] & \text{for } 0 \leq \frac{z-z_D}{z_{\text{TOA}}-z_D} \leq \frac{1}{2}, \\ -\frac{\alpha}{2}\left[1 + \left(\frac{z-z_D}{z_{\text{TOA}}-z_D} - \frac{1}{2}\right)\pi\right] & \text{for } \frac{1}{2} \leq \frac{z-z_D}{z_{\text{TOA}}-z_D} \leq 1, \end{cases} \tag{65}$$

where $z_{\text{TOA}} = 80.0\,\text{km}$, $z_D = 60.0\,\text{km}$, and $\alpha = 0.5$. A free-slip boundary condition is applied to the bottom boundary. Both the top and bottom boundary conditions are approximations of the physical boundaries of the atmosphere, and these may be sources of error. See Subsection 22.4 for more details on these choices of the top and bottom boundaries.

To increase the comparability of the numerical model with our asymptotic model following the discussion on the boundaries from Subsection 22.4, the results displayed from hereon will be limited to the vertical extent of $z \in [3.0\,\text{km}, 25.0\,\text{km}]$, although the simulation is computed on the full domain. Furthermore, the domain is periodic in the horizontal direction. The simulations in this section are conducted on a grid with $(N_x \times N_z) = (301 \times 120)$ grid points. See Appendix C for investigations involving other spatial resolutions.

For the initial perturbation in (59), the prognostic variables in the form of (12) are depicted in Figure 3.
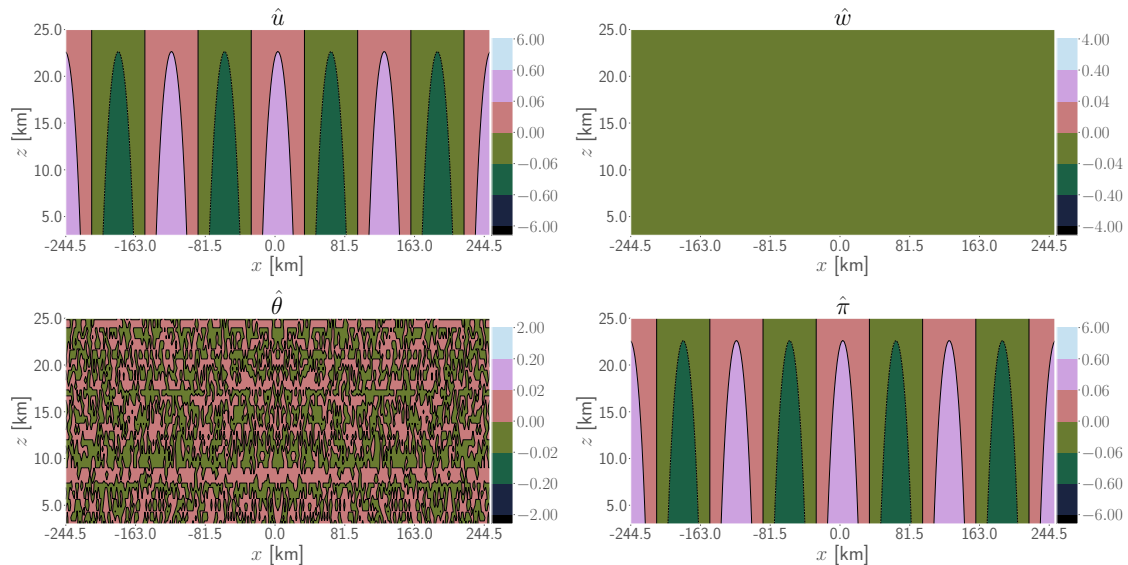
17

Figure 3: Initial perturbation: distribution of the prognostic variables with the transformation given in (12). (top left) Transformed horizontal velocity perturbation $\hat{u}$, (top right) transformed vertical velocity perturbation $\hat{w}$, (bottom left) transformed potential temperature perturbation $\hat{\theta}$, and (bottom right) transformed Exner pressure perturbation $\hat{\pi}$. The contours have the unit of $\mathrm{kg}^{1/2}\,\mathrm{m}^{-1/2}\,\mathrm{s}^{-1}$, i.e. the units of the square root of energy density.

4.3. Instability growth rate under the non-traditional setting

Two configurations of the perturbations are investigated below. One configuration involves the non-traditional setting with $\Omega_y = 7.292 \times 10^{-5}\,\mathrm{s}^{-1}$, and the other does not involve the effect of the Coriolis force, i.e. $\Omega = 0.0\,\mathrm{s}^{-1}$. The latter configuration is equivalent to the traditional approximation. The time-step size $\Delta t = 600.0\,\mathrm{s}$ is restricted by an advective Courant-Friedrichs-Lewy number of $\mathrm{CFL}_{\mathrm{adv}} = 0.9$. Appendix C contains results from runs with other time-step sizes.

The relative norm being a measure for the energy of the perturbation is given by

$$\text{rel. norm} = \frac{\|\hat{\boldsymbol{\psi}}\|}{\|\hat{\boldsymbol{\psi}}_0\|}, \tag{66}$$

where $\|\cdot\|$ represents the L^2-norm in (23), and $\hat{\boldsymbol{\psi}}_0$ denotes the initial $\hat{\boldsymbol{\psi}}$. Figure 4 depicts the change of the logarithm of the relative norm over time for the two configurations. Furthermore, a best-fit curve ($\mathscr{F}(t)$, black dashes) is plotted alongside the initial increment of the run with the non-traditional setting (red dotted solid curve). The best-fit curve is obtained by a least-square linear fit in the semi-logarithmic plot of Figure 4.

In Figure 4, the relative norm of the traditional approximation run (blue dotted dashed curve) is conserved, and the curve remains at 1.0 for over 6000 s. This is to be expected as the leading-order eigenvector is nothing but a Lamb wave in the traditional approx-
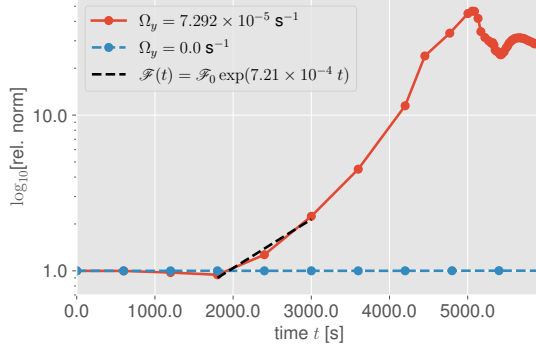
18

Figure 4: Semi-logarithmic plot of the relative norm against time: A run with the traditional approximation (blue dotted dashed curve); a run with the non-traditional setting (red dotted solid curve); and a best-fit curve (black dashes) of the initial increment in the run with the non-traditional setting.

imation which propagates indefinitely without change in the inviscid atmosphere. In contrast, the relative norm of the run with the non-traditional setting increases exponentially after approximately $1800\,\mathrm{s}$. The best-fit curve indicates that the experimental growth rate of the instability arising from the run with the non-traditional setting is $7.21 \times 10^{-4}\,\mathrm{s}^{-1}$, and this is remarkably close to the theoretically predicted instability growth rate of $7.85 \times 10^{-4}\,\mathrm{s}^{-1}$ from (63).
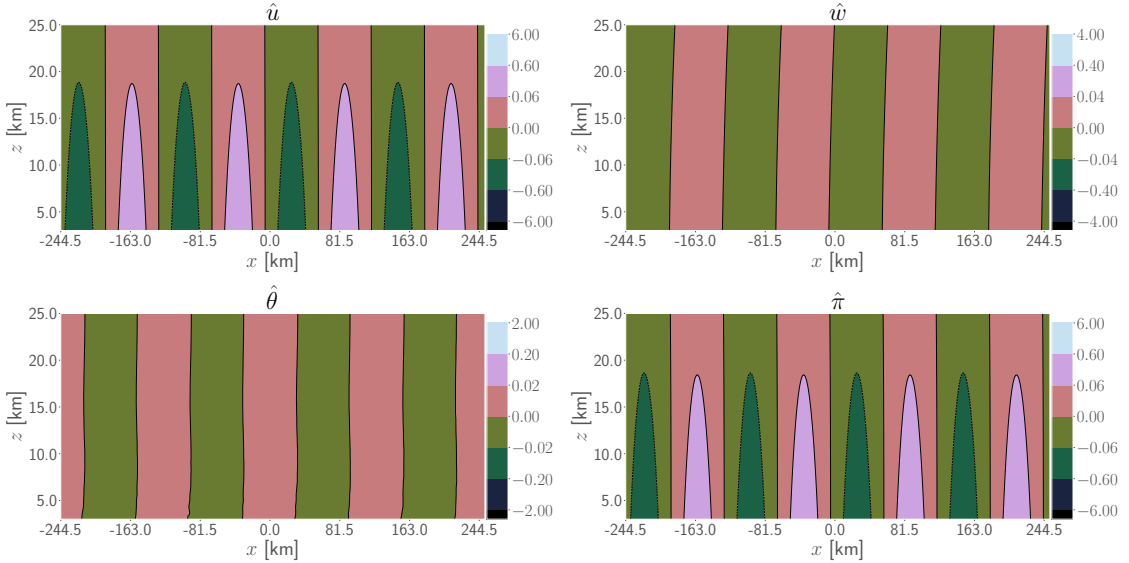

Figure 5: Output of the fields for the transformed prognostic variables at $t = 5.0\,\mathrm{hrs}$ for the configuration without the effect of the Coriolis force, i.e. $\boldsymbol{\Omega}_y = 0.0$ corresponding to the traditional approximation. Contour units are as in Figure 3.

Figures 5, 6, and 7 depict the fields of the transformed prognostic variables for the two

19

configurations of the wave perturbations. For the case with the traditional approximation in Figure 5, the fields depicted are at $18\,000\,\text{s} = 5.0\,\text{hrs}$ which is a significantly longer time scale in comparison with the time scale of the instability as measured, for instance, by the doubling rate of 15 min. Here we observe that, in comparison with Figure 3, some energy of the Lamb wave is lost as the amplitudes in $\hat{u}$ and $\hat{\pi}$ decrease slightly. The energy loss is most likely caused by numerical damping, as such an energy loss was also observed in simulation runs involving a free-slip upper boundary condition (not shown here) which satisfies the exact Lamb wave solution. This observation rules out any significant impact of the Rayleigh damping layer on the domain of interest. The amplitudes in the fields $\hat{w}$ and $\hat{\theta}$ remain negligibly small.

For the case with the non-traditional setting, Figure 6 depicts the fields at $3600\,\text{s} = 1.0\,\text{hr}$. At this point in time, the relative norm is arguably still of the order of magnitude of unity as shown in Figure 4. Therefore, the amplitude of the instability is small and its evolution is governed by linear or maybe weakly nonlinear theory. To ensure that we compare the numerical results with our linear theory from Section 2, we have chosen only the first few time steps starting with the onset of instability to compute the best-fit curve (see the black dashed plot in Figure 4).

For completeness, we include results on the non-linear instability in our numerical study. Figure 7 depicts the fields later in time at $5490\,\text{s} \approx 1.5\,\text{hrs}$. Referring to Figure 4, the relative norm of the perturbation has now grown by more than one order of magnitude from the initial condition. The evolution is clearly not governed by the linear regime anymore. Nonlinear effects cause fine-scale fast-mode oscillations that appear in the lower half of the domain. The results may depict the evolution from the linear to non-linear regime of the instability. The drop of the relative norm as seen in Figure 4 and consequentially the energy of the perturbation after approximately $5000\,\text{s}$ is most likely due to the nonlinear interaction with the mean flow. Energy is transferred from the instability to the mean flow resulting in an acceleration of the latter. Mean-flow acceleration also explains the tilt in lines of constant phase that can already be observed in Figure 6 due to a Doppler shift. Hence, it is more likely that the regime at $1.5\,\text{hrs}$ is already weakly nonlinear. The fine-scale structures in Figure 7 may eventually develop into turbulence.

In Appendix C, the experimental instability growth rate with the non-traditional setting is obtained for a range of spatial and temporal resolutions, and the results are compared to the theoretical instability growth rate.

5. Conclusions

This paper presents a novel instability that arises from considering a complete representation of the Coriolis force. This instability lends itself to physical interpretations and may have substantial implications for numerical schemes that employ the non-traditional approximation.

Considering the linearised compressible Euler equations in the non-traditional setting, an inner product of the state vector of the prognostic variables for perturbations is de-
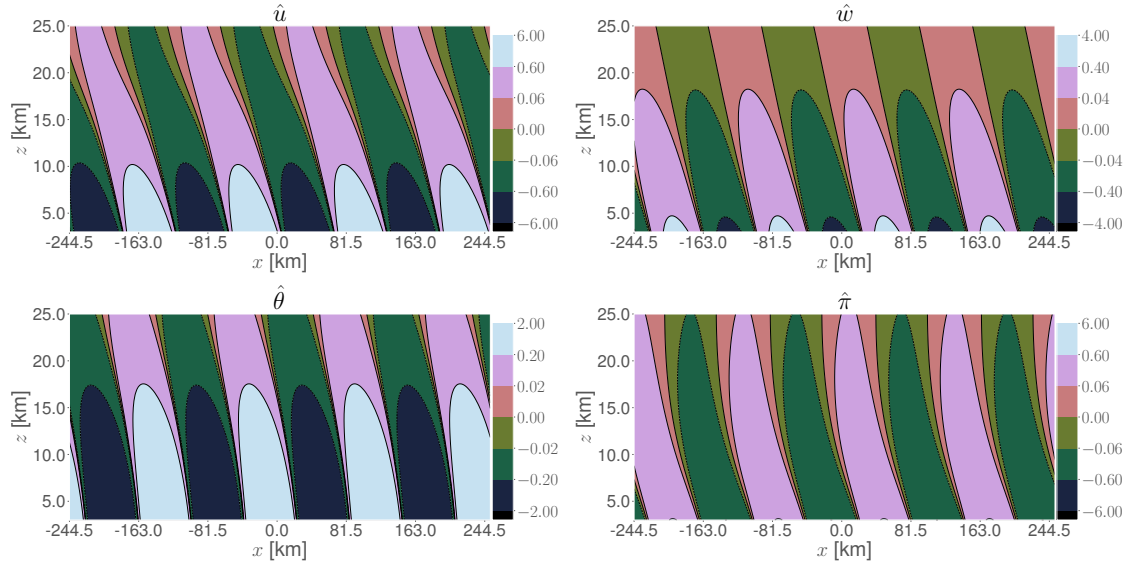
Figure 6: Output of the fields for the transformed prognostic variables at $t = 1.0\,\mathrm{hrs}$ for the configuration with the non-traditional setting, i.e. $\Omega_y = 7.292 \times 10^{-5}\,\mathrm{s}^{-1}$. Contour units are as in Figure 3.

Figure 7: Output of the fields for the transformed prognostic variables at $t \approx 1.5\,\mathrm{hrs}$ for the configuration with the non-traditional setting, i.e. $\Omega_y = 7.292 \times 10^{-5}\,\mathrm{s}^{-1}$. Contour units are as in Figure 3.
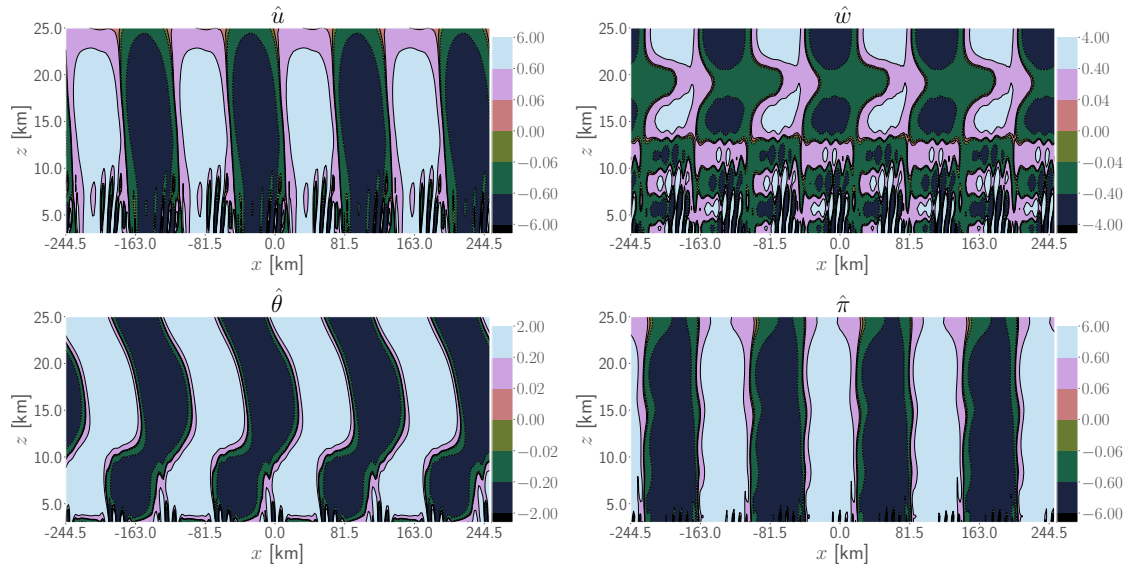
rived inducing a norm. We showed that this norm is equivalent to the perturbation's total energy. We found that the differential operator emerging from the linear system, after the usual separation of variables, is not skew-Hermitian with respect to the in-

ner product when the top boundary is non-reflecting. By some version of the spectral theorem, this observation gives rise to a potentially unstable spectrum. And indeed, by means of asymptotic theory, we showed that the isothermal, hydrostatic atmosphere at rest subject to the full Coriolis acceleration at the equator becomes unstable under infinitesimal initial perturbations. The theoretical growth rate of the instability is quantified.

With a small perturbation of the isothermal hydrostatic atmosphere at rest, numerical experiments demonstrate that this initial configuration becomes linearly unstable when the full Coriolis acceleration is considered. The experimental instability growth rate is close to the theoretical value. In contrast, the simulation remains stable if the traditional approximation is applied. Appendix C contains further investigations in this direction involving simulation runs in the non-traditional setting with varying spatial and temporal resolutions. The numerical experiments also revealed that the instability accelerates the mean flow. As a consequence, it can be speculated that the Lamb-wave-like instability may potentially influence atmospheric circulation.

Physical evidence from observations for this novel type of instability can be found in Nishida et al. [2014]. They observed Lamb waves at around 30° North, arguably close to the equator, with a vast array of high-resolution microbarometers. In contrast to intermittent waves due to large-scale events such as volcanic eruptions, they found omnipresent background waves. The authors discuss several excitation mechanisms as a cause for the phenomenon observed. Our results imply that these Lamb waves might be generated by the instability due to the Coriolis force, as the frequency spectrum of the observations fits well with our theoretical predictions. Further corroboration is that most waves the authors observed travel along the East-West axis as predicted by our theory.

Furthermore, our investigation presents relevant implications for non-traditional numerical models. Given the free surface top boundary, which is usually employed as a "sponge" layer in weather and climate models, one would encounter this instability in numerical simulations. This effect would be especially significant for the numerical simulations of the deep atmosphere, e.g. the papers by Borchert et al. [2019], Smolarkiewicz et al. [2016] as mentioned above, or tropical dynamics with the non-traditional setting. Therefore, the characterisation of the instability presented here is a worthwhile pursuit.

Our derivation of the instability and the numerical experiments have three significant limitations. 1) The β-plane effect has been neglected, 2) the effect of the Earth's curvature has not been considered, and 3) only two spatial dimensions were considered. The developments presented in this paper will benefit from a future study that overcome these limitations. An exhaustive study of the physical interpretations of the instability could also be carried out.

Concerning limitations 1) and 3), we may use scale analysis to provide an estimate for the influence of the β-plane effect as follows. By some Wentzel-Kramers-Brillouin-type argument, we may assume that the perturbation is meridionally homogeneous if it remains relatively constant within a latitude range of 10 wavelengths. With the setting used in the numerical experiments, the wavelength is approximately $125\,\mathrm{km}$. Let us now compute the rate of the β-plane effect due to the term $f' = \beta y$ at the northern edge of a

meridional domain of size $1250\,\text{km}$. Taking $\beta = 2\Omega/a$ at the equator where a represents the Earth's radius, this amounts to $f' \approx 1 \times 10^{-5}\,\text{s}^{-1}$. As the β-plane effect is linear in the governing equations, we may compare it with the theoretical growth rate obtained from linear stability analysis. From (63), this is approximately $8 \times 10^{-4}\,\text{s}^{-1}$ which is about 80 times greater than f'. Hence, damping of the perturbation might be possible due to the β-plane effect but with a damping rate that is, nevertheless, almost two orders of magnitude smaller than the instability growth rate. We anticipate that the inclusion of the β-plane approximation will have only a small effect on the theory and results presented in this paper.

Finally, it may also be fruitful to investigate this instability in the more operationally-ready numerical models at the German Weather Service (DWD) and the European Centre for Medium-Range Weather Forecasts (ECMWF). Two questions are particular worth answering. Can the instability described in this paper be reproduced by the numerical models? If the answer is yes, what influences does the instability have on atmospheric dynamics and circulation?

Acknowledgments

Data availability statement

The data sets and scripts used to generate the numerical results in Section 4 and Appendix C are available on *zenodo.org* [Chew et al., 2022b]. The supplementary material also includes, for each simulation run from Appendix C, numerical results similar to those presented in Section 4. These additional results may be generated from the accompanying data sets and scripts.

The source code for the numerical model presented in Section 3 is hosted on the Freie Universität Berlin (FUB)'s GitLab page. Currently, access to the repository is limited to users with an FUB account due to privacy concerns and can be granted on a case-by-case basis by contacting R.C. at ray.chew@fu-berlin.de.

A. The Coriolis force

At a certain latitude represented by Φ, the full Coriolis force on the Earth's surface is given by a titled vector with magnitude 2Ω. This may be written as a sine term perpendicular to the surface, and a cosine term that is parallel. The traditional approximation ignores contributions from the cosine terms.
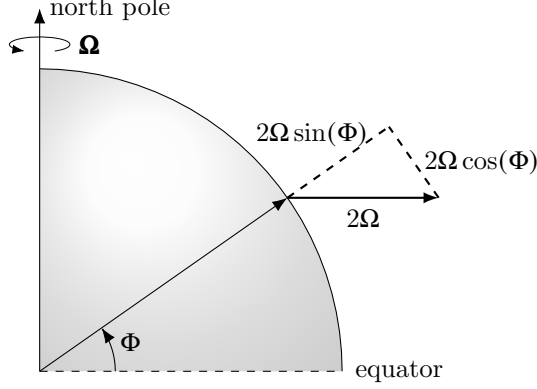

Figure 8: An illustration of the effect of the full Coriolis acceleration acting on the Earth's surface at a latitude Φ. An explanation is provided in the accompanying text.

Thuburn et al. [2002] introduced the f-F-plane approximation that is analogous to the non-traditional approximation. Here, $f = 2\Omega\sin(\Phi)$ and $F = 2\Omega\cos(\Phi)$. The β-plane approximation extends f-plane by including its latitudinal dependence, i.e.,

$$f_\beta = f + f' = f + \beta y, \tag{67}$$

with $\beta = (\mathrm{d}f/\mathrm{d}y)|_\Phi = 2\Omega\cos(\Phi)/a$, where y is the meridional distance and a is the Earth's radius. In this paper, we consider the atmosphere at the equator with the f-plane approximation only. The β-plane approximation is neglected.

B. Extension of the numerical model to support the non-traditional setting

B.1. Semi-implicit integration of the stiff terms

The stiff terms in (47) are integrated by the implicit trapezoidal rule in time. Thus an explicit Euler step at the start of the time step is followed, after advection, by an implicit Euler step to complete a full-time update step. The implicit Euler scheme is also invoked in predicting the advective half-time level fluxes $(P\boldsymbol{v})^{n+1/2}$ in (56). The crucial implicit Euler step, and an extension to support the non-traditional setting, is described in this Appendix.

As (47a) and (47d) are free of stiff terms, ρ and P are unchanged during the present implicit step. As a consequence, we have

$$\frac{\partial U}{\partial t} = -c_p (P\theta)^\circ \frac{\partial \pi'}{\partial x} - \left(2\,\Omega_y W - 2\,\Omega_z V\right), \tag{68a}$$

$$\frac{\partial V}{\partial t} = -c_p (P\theta)^\circ \frac{\partial \pi'}{\partial y} - \left(2\,\Omega_z U - 2\,\Omega_x W\right), \tag{68b}$$

$$\frac{\partial W}{\partial t} = -c_p (P\theta)^\circ \frac{\partial \pi'}{\partial z} - g\frac{\tilde{\chi}}{\chi^\circ} - \left(2\,\Omega_x V - 2\,\Omega_y U\right), \tag{68c}$$

$$\frac{\partial \tilde{\chi}}{\partial t} = -W\frac{\mathrm{d}\bar{\chi}}{\mathrm{d}z}, \tag{68d}$$

$$\left(\frac{\partial P}{\partial \pi}\right)^\circ \frac{\partial \pi'}{\partial t} = -\frac{\partial U}{\partial x} - \frac{\partial V}{\partial y} - \frac{\partial W}{\partial z}, \tag{68e}$$

where $(U, V, W, \tilde{\chi}) = (Pu, Pv, Pw, P\chi')$, and $(P\theta)^\circ$, χ°, and $(\partial P/\partial \pi)^\circ$ are the data available when the implicit Euler solver is invoked. The Earth's angular velocity vector $\mathbf{\Omega} = \Omega_x \boldsymbol{e}_x + \Omega_y \boldsymbol{e}_y + \Omega_z \boldsymbol{e}_z$ is written in the zonal, meridional, and vertical components. In the temporal semi-discretisation, this solver integrates

$$U^{n+1} = U^n - \Delta t \left[c_p (P\theta)^\circ \frac{\tilde{\partial}\pi'^{n+1}}{\tilde{\partial}x} + \left(2\,\Omega_y W^{n+1} - 2\,\Omega_z V^{n+1}\right) \right], \tag{69a}$$

$$V^{n+1} = V^n - \Delta t \left[c_p (P\theta)^\circ \frac{\tilde{\partial}\pi'^{n+1}}{\tilde{\partial}y} + \left(2\,\Omega_z U^{n+1} - 2\,\Omega_x W^{n+1}\right) \right], \tag{69b}$$

$$W^{n+1} = W^n - \Delta t \left[c_p (P\theta)^\circ \frac{\tilde{\partial}\pi'^{n+1}}{\tilde{\partial}z} + g\frac{\tilde{\chi}^{n+1}}{\chi^\circ} + \left(2\,\Omega_x V^{n+1} - 2\,\Omega_y U^{n+1}\right) \right], \tag{69c}$$

$$\tilde{\chi}^{n+1} = \tilde{\chi}^{n+1} - \Delta t \frac{\tilde{\mathrm{d}}\bar{\chi}}{\tilde{\mathrm{d}}z} W^{n+1}, \tag{69d}$$

$$\left(\frac{\tilde{\partial}P}{\tilde{\partial}\pi}\right)^\circ \pi'^{n+1} = \left(\frac{\tilde{\partial}P}{\tilde{\partial}\pi}\right)^\circ \pi'^n - \Delta t \left(\frac{\tilde{\partial}U^{n+1}}{\tilde{\partial}x} - \frac{\tilde{\partial}V^{n+1}}{\tilde{\partial}y} - \frac{\tilde{\partial}W^{n+1}}{\tilde{\partial}z}\right). \tag{69e}$$

We note that the explicit Euler step in (58a) entails solving (69) with the time level $n+1$ replaced by the time level n everywhere on the right-hand side of (69).

Now we let

$$\nu = \Delta t\,N, \quad \omega_m = 2\,\Delta t\,\Omega_m, \quad m \in \{x, y, z\}, \tag{70}$$

with the local buoyancy frequency

$$N = \sqrt{-g\frac{1}{\chi^\circ}\frac{\mathrm{d}\bar{\chi}}{\mathrm{d}z}} \tag{71}$$

in (13) now written in terms of the inverse potential temperature χ. Furthermore, we let

$$\boldsymbol{U} = \begin{pmatrix} U \\ V \\ W \end{pmatrix}, \quad \boldsymbol{F} = \begin{pmatrix} 0 & -\omega_z & \omega_y \\ \omega_z & 0 & -\omega_x \\ -\omega_y & \omega_x & \nu^2 \end{pmatrix}, \quad \text{and} \quad \boldsymbol{H} = \boldsymbol{I} + \boldsymbol{F}, \tag{72}$$

where $\boldsymbol{I}$ is the identity matrix. Then the equation for the advective fluxes $(U, V, W)^{n+1}$ in (69), after the insertion of (69d) in (69c), can be recast as,

$$\boldsymbol{A}_w U^{n+1} = U^{n*} - \boldsymbol{F}\,\boldsymbol{U}^{n+1} - \Delta t\, c_p (P\theta)^\circ \tilde{\nabla}\pi', \tag{73}$$

or, equivalently,

$$\boldsymbol{U}^{n+1} = \boldsymbol{H}^{-1}\left(\boldsymbol{U}^{n*} - \Delta t\, c_p (P\theta)^\circ \tilde{\nabla}\pi'\right), \tag{74}$$

where

$$\boldsymbol{U}^{n*} = \left(U^n, V^n, W^n - \Delta t\, g\frac{\tilde{\chi}^n}{\chi^\circ}\right)^T. \tag{75}$$

We note that

$$\boldsymbol{H} = \begin{pmatrix} 1 & -\omega_z & \omega_y \\ \omega_z & 1 & -\omega_x \\ -\omega_y & \omega_x & 1+\nu^2 \end{pmatrix} \tag{76}$$

and

$$\det(\boldsymbol{H}) = \omega_x^2 + \omega_y^2 + (1+\nu^2)(1+\omega_z^2). \tag{77}$$

The inversion of $\boldsymbol{H}$ leads to

$$\boldsymbol{H}^{-1} = \frac{1}{\det(\boldsymbol{H})} \begin{pmatrix} (1+\nu^2)+\omega_x^2 & (1+\nu^2)\omega_z+\omega_x\omega_y & -\omega_y+\omega_z\omega_x \\ -(1+\nu^2)\omega_z+\omega_x\omega_y & (1+\nu^2)+\omega_y^2 & \omega_x+\omega_y\omega_z \\ \omega_y+\omega_z\omega_x & -\omega_x+\omega_y\omega_z & 1+\omega_z^2 \end{pmatrix}. \tag{78}$$

Insertion of (74) into the pressure equation (69e) leads to a closed Helmholtz-type equation for π'^{n+1},

$$\left(\frac{\tilde{\partial}P}{\tilde{\partial}\pi}\right)^\circ \pi'^{n+1} - \Delta t^2\, \tilde{\nabla}\cdot\left[\boldsymbol{H}^{-1}c_p(P\theta)^\circ\tilde{\nabla}\pi'^{n+1}\right] = \left(\frac{\tilde{\partial}P}{\tilde{\partial}\pi}\right)^\circ \pi'^{n} - \Delta t\, \tilde{\nabla}\cdot\left(\boldsymbol{H}^{-1}\boldsymbol{U}^{n*}\right). \tag{79}$$

After its solution, backward re-insertion into (69a)–(69d) yields $(U, V, W, \tilde{\chi})^{n+1}$. Details on computing the spatial derivatives on the right-hand side of (69) are deferred to Section 4c3 of Benacchio and Klein [2019].

B.2. Solving for the Exner pressure perturbation increment

For implementation purposes, we introduce the option of explicitly using the decomposition

$$\pi'^{n+1} = \pi'^{n} + \delta\pi, \tag{80}$$

such that only the time increment of the Exner pressure perturbation is updated in the solution of the Helmholtz-type problem in (79). Solution of the time increment only may improve the accuracy of the iterative solver for small time increments.

With the decomposition in (80), (79) may be written as

$$\left(\frac{\tilde{\partial}P}{\tilde{\partial}\pi}\right)^\circ \delta\pi - \Delta t^2\, \tilde{\nabla}\cdot\left[\boldsymbol{H}^{-1}c_p(P\theta)^\circ\tilde{\nabla}\delta\pi\right] = -\Delta t\, \tilde{\nabla}\cdot\left(\boldsymbol{H}^{-1}\boldsymbol{U}^{n**}\right), \tag{81}$$

where
$$\boldsymbol{U}^{n**} = \boldsymbol{U}^{n*} - \Delta t \, c_p (P\theta)^\circ \tilde{\nabla} \pi'^{n}. \tag{82}$$

Upon obtaining the solution of $\delta\pi$, re-insertion into (80) recovers π^{n+1}.

C. The instability growth rate under varying spatial and temporal resolutions

The instability growth rate of the wave perturbation with the non-traditional setting is computed for the following spatial resolutions ($N_x \times N_z$):

$$(151 \times 60); \quad (301 \times 120); \quad (601 \times 240); \quad (1201 \times 480).$$

Furthermore for each spatial resolution of the grid, runs with the following time-step sizes Δt are made:

$$\Delta t = (200, 400, 600, 800, 1000, 1200, 1400, 1600) \, \text{s}.$$

Finally, a best-fit curve similar to the one presented in Figure 4 is obtained for the initial increment of the relative norm. This interval corresponds to the linear regime of the instability growth and should be the closest to the theoretical instability growth rate in (63).

For a particular spatial and temporal resolution, the best-fit curve is given by

$$\mathscr{F}(t) = \mathscr{F}_0 \exp(\zeta \, t), \tag{83}$$

where $\mathscr{F}_0$ and ζ are obtained from the curve-fitting method. The values of ζ obtained from runs with the spatial and temporal resolutions above are presented in Figure 9. The colour map is divided by the variation of the computed instability growth rate from the theoretical value. Specifically, the ζ-values that fall within $\pm 10\%$ of the theoretical 7.85×10^{-4} are shaded in light yellow, e.g., (151×60) with $\Delta t = 1400.0 \, \text{s}$. The ζ-values within $+(-) \, 25\%$ of the theoretical ζ are shaded in light orange, and so on. In Figure 9, values of ζ are omitted when the CFL_{adv} constraint dominates, and increasing the time-step size has no further effect on the simulation result. This scenario occurs for, e.g., (1201×480) with time-step sizes $\Delta t \geq 800.0 \, \text{s}$.

The task of estimating the instability growth rate is difficult and may be sensitive to the experimental parameters [McNally et al., 2012, Zhelyazkov, 2015]. Yet 16 out of the 25 runs with varying spatial and temporal resolutions produce an experimental ζ value that fall within $\pm 50\%$ of the value from the theoretical instability growth rate. Moreover, the error introduced via the instability remains of the same order of magnitude over all spatial and temporal resolutions investigated. These encouraging results corroborate the theory developed in Section 2. The result presented in Figure 9 extends the numerical experiments in Section 4 to more than one set of spatial and temporal resolutions. For the numerical simulations presented in this Appendix, results similar to the ones presented Section 4 may be found in the supplementary material to this manuscript [Chew et al., 2022b].
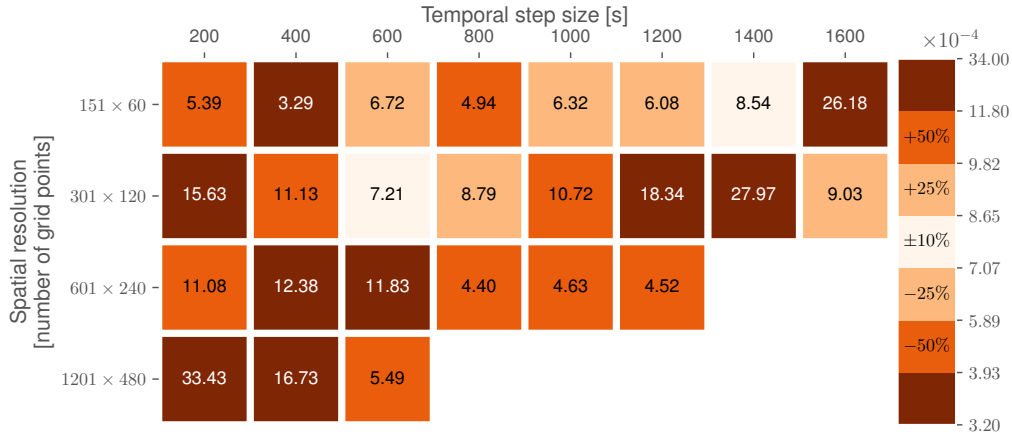
Temporal step size [s]

Spatial resolution [number of grid points]	200	400	600	800	1000	1200	1400	1600
151×60	5.39	3.29	6.72	4.94	6.32	6.08	8.54	26.18
301×120	15.63	11.13	7.21	8.79	10.72	18.34	27.97	9.03
601×240	11.08	12.38	11.83	4.40	4.63	4.52		
1201×480	33.43	16.73	5.49					

$\times 10^{-4}$: 34.00, 11.80, +50%, 9.82, +25%, 8.65, ±10%, 7.07, −25%, 5.89, −50%, 3.93, 3.20

Figure 9: Heat map of the ζ-values for varying spatial and temporal resolutions. Refer to the text and (83) for the explanation of ζ. Note that the values depicted have a factor of 10^{-4}. The colour map depicts the variation of ζ from the theoretical 7.85×10^{-4}. Darker shades represent a larger variation and vice versa.

References

U. Achatz. *Atmospheric Dynamics*. Springer Berlin Heidelberg, 1 edition, 2022.

U. Achatz, R. Klein, and F. Senf. Gravity waves, scale asymptotics and the pseudo-incompressible equations. *J. Fluid Mech.*, 663:120–147, Nov. 2010. ISSN 0022-1120, 1469-7645. doi: 10.1017/S0022112010003411.

T. Benacchio and R. Klein. A semi-implicit compressible model for atmospheric flows with seamless access to soundproof and hydrostatic dynamics. *Mon. Wea. Rev.*, 147: 4221–4240, 2019. doi: 10.1175/MWR-D-19-0073.1.

T. Benacchio, W. P. O'Neill, and R. Klein. A blended soundproof-to-compressible numerical model for small-to mesoscale atmospheric dynamics. *Mon. Wea. Rev.*, 142: 4416–4438, 2014. doi: 10.1175/MWR-D-13-00384.1.

S. Borchert, G. Zhou, M. Baldauf, H. Schmidt, G. Zängl, and D. Reinert. The upper-atmosphere extension of the ICON general circulation model (version: Ua-icon-1.0). *Geosci. Model Dev.*, 12(8):3541–3569, Aug. 2019. ISSN 1991-9603. doi: 10.5194/gmd-12-3541-2019.

R. Chew, T. Benacchio, G. Hastermann, and R. Klein. A one-step blended soundproof-compressible model with balanced data assimilation: theory and idealised tests. *Monthly Weather Review*, 2022a. In press.

R. Chew, M. Schlutow, and R. Klein. Supplementary material for "Instability of the isothermal, hydrostatic equatorial atmosphere at rest under the full Coriolis acceleration", May 2022b. URL https://doi.org/10.5281/zenodo.6585508.

A. Colin de Verdière and R. Schopp. Flows in a rotating spherical shell: the equatorial case. *J. Fluid Mech.*, 276:233–260, 1994. doi: 10.1017/S0022112094002545.

G. G. Coriolis. *Mémoire sur les équations du mouvement relatif des systèmes de corps.* J. Éc. Polytech. Paris, 1835.

D. R. Durran. Improving the Anelastic Approximation. *Journal of the Atmospheric Sciences*, 46(11):1453–1461, June 1989. ISSN 0022-4928, 1520-0469. doi: 10.1175/ 1520-0469(1989)046⟨1453:ITAA⟩2.0.CO;2.

D. R. Durran. *Numerical methods for fluid dynamics: With applications to geophysics.* Springer, 2 edition, 2010.

D. R. Durran and J. B. Klemp. A compressible model for the simulation of moist mountain waves. *Monthly Weather Review*, 111(12):2341–2361, 1983. doi: 10.1175/ 1520-0493(1983)111⟨2341:ACMFTS⟩2.0.CO;2.

C. Eckart. *Hydrodynamics of Oceans and Atmospheres.* Pergamon, New York, 1960.

M. D. Fruman. Equatorially Bounded Zonally Propagating Linear Waves on a Generalized β-Plane. *Journal of the Atmospheric Sciences*, 66(9):2937–2945, Sept. 2009. ISSN 1520-0469, 0022-4928. doi: 10.1175/2009JAS2932.1.

M. D. Fruman and T. G. Shepherd. Symmetric Stability of Compressible Zonal Flows on a Generalized Equatorial β-Plane. *Journal of the Atmospheric Sciences*, 65(6): 1927–1940, June 2008. ISSN 1520-0469, 0022-4928. doi: 10.1175/2007JAS2582.1.

T. Gerkema, J. T. F. Zimmerman, L. R. M. Maas, and H. van Haren. Geophysical and astrophysical fluid dynamics beyond the traditional approximation. *Rev. Geophys.*, 46 (2):RG2004, May 2008. ISSN 8755-1209. doi: 10.1029/2006RG000220.

T. Kato. *A Short Introduction to Perturbation Theory for Linear Operators.* Springer US, New York, NY, 1982. ISBN 978-1-4612-5702-8 978-1-4612-5700-4. doi: 10.1007/ 978-1-4612-5700-4.

P.-S. Laplace. *Oeuvres complètes de Laplace*, volume 6. Gauthier-Villars, Paris, 1835.

V. B. Lidskii. Perturbation theory of non-conjugate operators. *USSR Computational Mathematics and Mathematical Physics*, 6(1):73–85, Jan. 1966. ISSN 0041-5553. doi: 10.1016/0041-5553(66)90033-4.

L. R. Maas and U. Harlander. Equatorial wave attractors and inertial oscillations. *J. Fluid Mech.*, 570:47–67, 2007. doi: 10.1017/S0022112006002904.

C. P. McNally, W. Lyra, and J.-C. Passy. A well-posed Kelvin-Helmholtz instability test and comparison. *Astrophys. J., Suppl. Ser.*, 201(2):18, 2012. doi: 10.1088/0067-0049/ 201/2/18.

K. Nishida, N. Kobayashi, and Y. Fukao. Background Lamb waves in the Earth's atmosphere. *Geophysical Journal International*, 196(1):312–316, Jan. 2014. ISSN 1365-246X, 0956-540X. doi: 10.1093/gji/ggt413.

J. Pedlosky. *Geophysical Fluid Dynamics*. Springer, 2 edition, 2013.

M. Rodal and M. Schlutow. Waves in the gas centrifuge: Asymptotic theory and similarities with the atmosphere. *J. Fluid Mech.*, 928:A17, Dec. 2021. ISSN 0022-1120, 1469-7645. doi: 10.1017/jfm.2021.811.

P. K. Smolarkiewicz, C. Kühnlein, and N. P. Wedi. A consistent framework for discrete integrations of soundproof and compressible PDEs of atmospheric dynamics. *J. Comput. Phys.*, 263:185–205, 2014. doi: 10.1016/j.jcp.2014.01.031.

P. K. Smolarkiewicz, W. Deconinck, M. Hamrud, C. Kühnlein, G. Mozdzynski, J. Szmelter, and N. P. Wedi. A finite-volume module for simulating global all-scale atmospheric flows. *Journal of Computational Physics*, 314:287–304, June 2016. ISSN 00219991. doi: 10.1016/j.jcp.2016.03.015.

J. Thuburn, N. Wood, and A. Staniforth. Normal modes of deep atmospheres. II: F-F-plane geometry. *Q. J. R. Meteorol. Soc.*, 128(584):1793–1806, July 2002. ISSN 00000000, 00359009. doi: 10.1256/003590002320603412.

G. K. Vallis. *Atmospheric and Oceanic Fluid Dynamics: Fundamentals and Large-Scale Circulation*. Cambridge University Press, 2 edition, 2017.

R. L. Walterscheid. A reexamination of evanescent acoustic-gravity waves: Special properties and aeronomical significance. *J. Geophys. Res.*, 108(D11):4340, 2003. ISSN 0148-0227. doi: 10.1029/2002JD002421.

A. A. White and R. A. Bromley. Dynamically consistent, quasi-hydrostatic equations for global models with a complete representation of the Coriolis force. *Q.J Royal Met. Soc.*, 121(522):399–418, Jan. 1995. ISSN 00359009, 1477870X. doi: 10.1002/qj.49712152208.

G. Zängl, D. Reinert, P. Rípodas, and M. Baldauf. The ICON (ICOsahedral Nonhydrostatic) modelling framework of DWD and MPI-M: Description of the nonhydrostatic dynamical core. *Q.J.R. Meteorol. Soc.*, 141(687):563–579, Jan. 2015. ISSN 00359009. doi: 10.1002/qj.2378.

I. Zhelyazkov. On modeling the Kelvin–Helmholtz instability in solar atmosphere. *J. Astrophys. Astron.*, 36(1):233–254, 2015. doi: 10.1007/s12036-015-9332-2.